

Predicting Mechanical Ventilation Requirement and Mortality in COVID-19 using Radiomics and Deep Learning on Chest Radiographs: A Multi-Institutional Study

Joseph Bae^{1,2*}, Saarthak Kapse^{3*}, Gagandeep Singh⁴, Tej Phatak⁴, Jeremy Green⁴,
Nikhil Madan⁵, Prateek Prasanna¹
(* equal contribution)

¹Department of Biomedical Informatics, Stony Brook University, NY, USA

²Renaissance School of Medicine, Stony Brook University, NY, USA

³Department of Electrical Engineering, Indian Institute of Technology, Bombay, India

⁴Department of Radiology, Newark Beth Israel Medical Center, NJ, USA

⁵Department of Pulmonary Critical Care, Newark Beth Israel Medical Center, NJ, USA

Abstract

Objectives

To predict mechanical ventilation requirement and mortality using computational modeling of chest radiographs (CXR) for coronavirus disease 2019 (COVID-19) patients. We also investigate the relative advantages of deep learning (DL), radiomics, and DL of radiomic-embedded feature maps in predicting these outcomes.

Methods

This two-center, retrospective study analyzed deidentified CXRs taken from 514 patients suspected of COVID-19 infection on presentation at Stony Brook University Hospital (SBUH) and Newark Beth Israel Medical Center (NBIMC) between the months of March and June 2020. A DL segmentation pipeline was developed to generate masks for both lung fields and artifacts for each CXR. Machine learning classifiers to predict mechanical ventilation requirement and mortality were trained and evaluated on 353 baseline CXRs taken from COVID-19 positive patients. A novel radiomic embedding framework is also explored for outcome prediction.

Results

Classification models for mechanical ventilation requirement (test N=154) and mortality (test N=190) had AUCs of up to 0.905 and 0.926, respectively. We also found that the inclusion of radiomic-embedded maps improved DL model predictions of clinical outcomes.

Conclusions

We demonstrate the potential for computerized analysis of baseline CXR in predicting disease outcomes in COVID-19 patients. Our results also suggest that radiomic embedding improves DL models in medical image analysis, a technique that might be explored further in other pathologies. The models proposed in this study and the prognostic information they provide, complementary to other clinical data, might be used to aid physician decision making and resource allocation during the COVID-19 pandemic.

Key Words: COVID-19, X-Ray, Deep learning, Machine learning, Artificial Intelligence

Key Points

- Computational modeling of baseline CXR can predict mechanical ventilation requirement and mortality with high sensitivity.
- Radiomic-embedded feature maps can improve modeling of outcomes in COVID-19 patients.

Introduction

Coronavirus disease 2019 (COVID-19), an illness caused by novel severe acute respiratory syndrome coronavirus 2, has spread rapidly across the world with over 9.5 million cases internationally and over 2.4 million cases in the United States as of June 25, 2020 [1].

While the popularity of chest computed tomography (CT) in the early detection and monitoring of COVID-19 is growing in many countries such as China, hospitals in the United States employ chest radiographs (CXR) as the primary imaging modality for the monitoring of the disease [2–8]. CXRs are useful due to the speed, portability, and easy disinfection of radiography units. The American College of Radiology has suggested that CT be reserved for only severe cases of COVID-19 and strongly recommends the usage of portable radiography units to minimize spread of infection [8]. However, CXRs have lower resolution than CT images and provide 2-Dimensional (2D) rather than 3D representations of the lungs. Additionally, portable radiography units may result in non-uniform orientations and partial visual fields on images. These features of CXRs make them more difficult to interpret than CTs. Current reports suggest that radiologist diagnosis of COVID-19 from CXR has a sensitivity of 69% compared to a sensitivity of up to 97% on CT [4, 5, 7].

There is a growing need for methods to monitor and predict disease progression in COVID-19. In severe cases of the infection, patients may progress to hypoxemic respiratory failure and acute respiratory distress syndrome requiring mechanical ventilation [9]. In the United States, early projections forecasted a deficit in ventilators during the COVID-19 pandemic, indicating the importance of efficient resource management [10]. The ability to identify patients that might progress to critical illness beginning at clinical presentation will be invaluable in potential ventilator shortages, and a few studies have demonstrated that radiologic imaging may be of use in this regard [3, 6, 11–13]. Recent studies have qualitatively described the association of ground-glass opacities and lung consolidations with disease presence and progression on CXR and CT [2–4, 6, 7]. Specifically, the presence of opacities in multiple lobes has been shown to predict severe illness [3]. Studies have also evaluated various clinical biomarkers and comorbidities as predictors of disease progression, and there is some evidence that imaging data might complement these models [6, 13–17]. However, uses of CXRs have been largely qualitative, and there has been little work linking quantifiable CXR findings with patient outcomes in COVID-19. Nevertheless, portable radiography is an appealing, and often the only modality in high-volume hospital settings. In this study we utilize computational techniques to further evaluate the role of CXR in predicting patient outcomes.

Computational radiology is a rapidly advancing field that employs machine learning to interpret medical images. Two general approaches include deep learning (DL) and radiomic analysis [12,

18]. Recent studies have used these techniques in order to study COVID-19, but few have applied them to multi-institutional CXR cohorts [2, 12, 19, 20]. Furthermore, there has not been extensive work utilizing computational models to predict COVID-19 outcomes using CXR.

In this study, we use computational techniques to identify clinically actionable information from CXR. We first predict both mechanical ventilation requirement and mortality from baseline CXR using a DL model. Our second experiment uses machine learning classifiers to predict these same outcomes based upon computer-extracted, pre-defined radiomic features. Third, we propose a combined DL model using both processed CXRs and corresponding radiomic-embedded feature maps as inputs to predict outcomes. This synergistic approach utilizing radiomic-embedded maps for DL has not been explored in evaluating CXRs and may offer insights into novel interpretations of pre-defined radiomic features. Figure 1 displays a general flowchart of experiments.

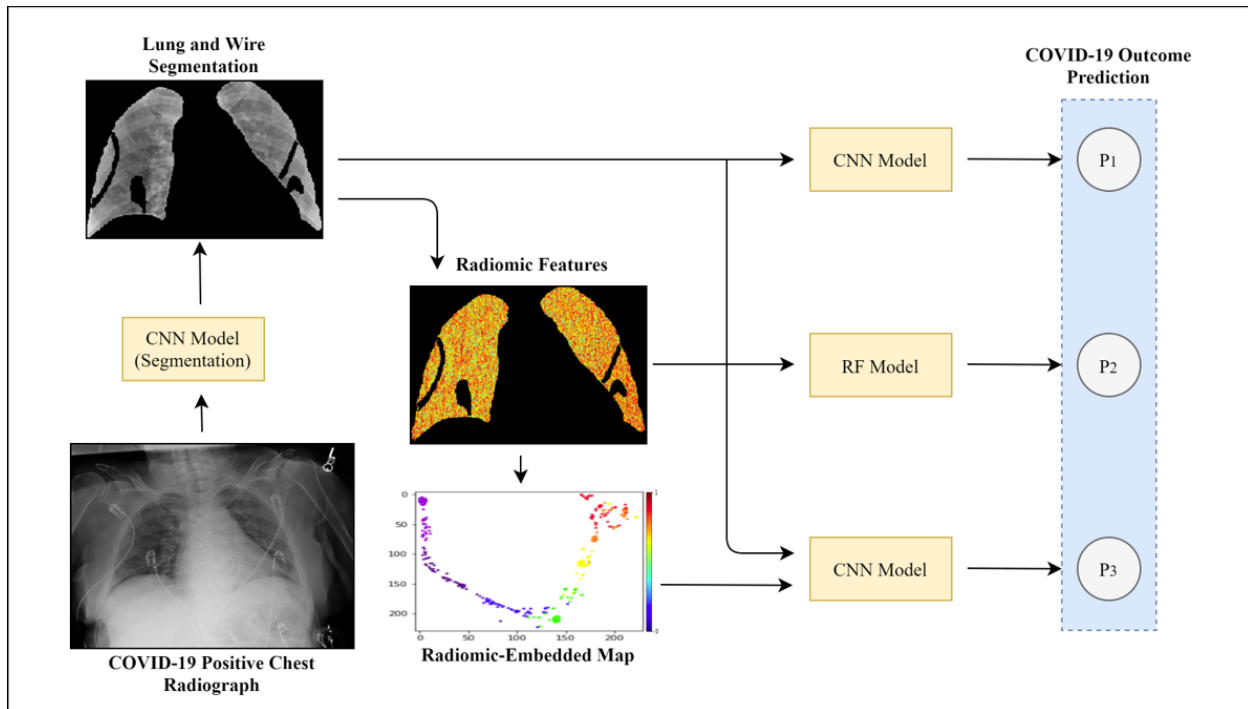


Figure 1: Study pipeline. Visualized here is the schema for the experiments performed in this study. Experiment 1 uses a CNN deep learning model to predict COVID-19 patient outcomes using segmented CXRs as inputs. In Experiment 2 we extract pre-defined radiomic features from segmented CXRs and input them into machine learning models such as Random Forests. In Experiment 3 we use extracted radiomic features to generate radiomic-embedded maps which are inputted with segmented CXRs into a CNN deep learning model.

Materials and Methods

Patient and Image Dataset

In this two-center, IRB approved study, anonymized coronal CXRs were obtained from patients suspected of COVID-19 on presentation at Stony Brook University Hospital (SBUH) and Newark Beth Israel Medical Center (NBIMC) between March and June 2020 (Figure 2). At SBUH, 484 baseline CXRs for 463 patients were analyzed. Among these, 17 CXRs from 16 patients were

discarded due to being images of pediatric patients or due to poor image quality. Here, a baseline CXR refers to any CXR taken on the first day for which CXR data exists for a patient. A total of 72 baseline CXRs obtained from 72 patients prior to ventilation were included from NBIMC. Of these, 5 CXRs were discarded due to indistinguishable lung fields.

In total, 534 CXRs taken from 514 patients were analyzed in this study. 305 of these images were from 290 male patients and 229 were from 224 female patients. The mean age of patients studied was 54 years old (median=55 years, standard deviation=18.055 years, Table 1). COVID-19 positivity was tested for each patient via reverse transcriptase polymerase chain reaction (RT-PCR). 353 CXRs were taken from 338 patients who tested positive for COVID-19 (Table 2) and 181 CXRs were from 176 patients who were found to be negative. CXRs taken from COVID-19 positive patients were used in outcome prediction experiments whereas those from both COVID-19 positive and negative patients were used to build lung and artifact segmentation models. Of the 353 CXRs from positive patients, 113 baseline CXRs were taken for 109 patients that later required mechanical ventilation. 89 CXRs were from 84 patients who later died from the disease. Representative CXR images are displayed in Figure 3. Training of all machine learning models was performed on CXRs acquired at SBUH and evaluated using a combination of CXRs taken at both SBUH and NBIMC.

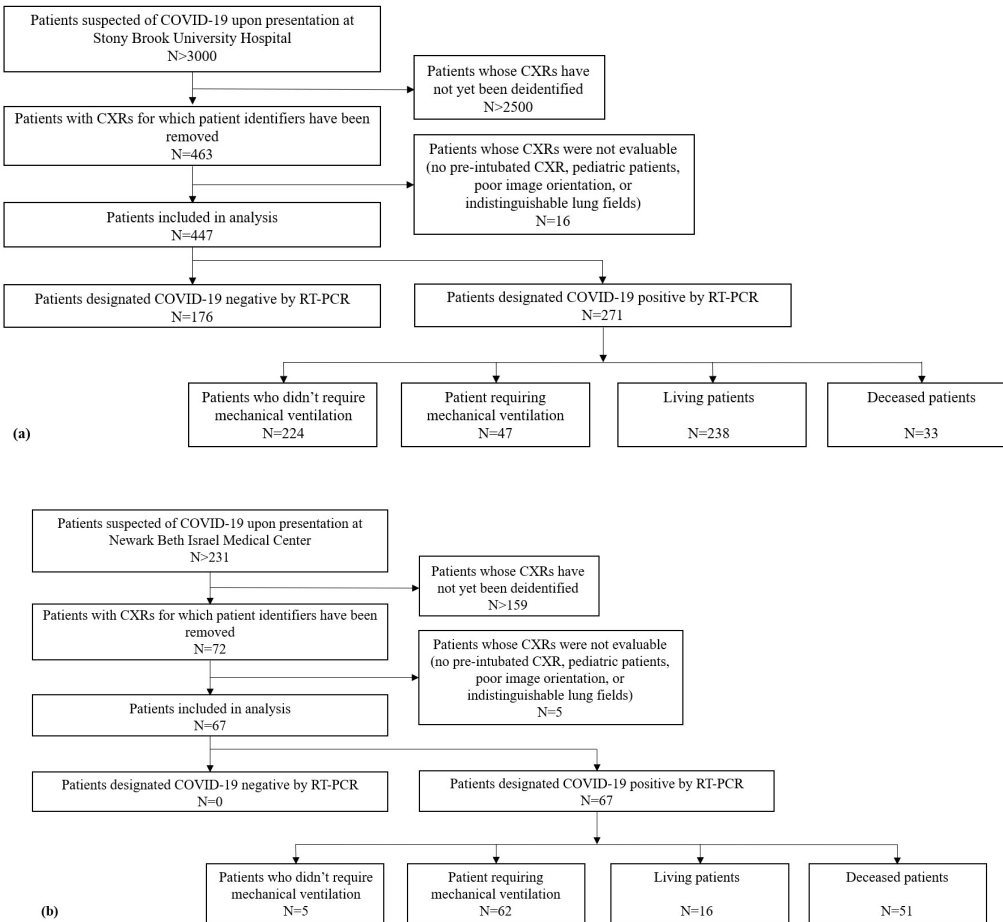


Figure 2. Summary of patient inclusion and exclusion criteria. (a) displays criteria for SBUH and (b) displays criteria for NBIMC

Table 1. Patient demographics table

	Stony Brook University Hospital patients (N=447)	Newark Beth Israel Medical Center patients (N=67)
Sex	248 male 199 female	42 male 25 female
Age	53±18.597 (p=0.6041*)	61±12.045 (p=0.5768*)

*p-values for age difference between sexes using a Wilcoxon rank-sum test

Image Preprocessing

To conduct our analysis, we ensured that CXRs were properly segmented to avoid analysis of features unrelated to lung fields. In order to segment the lungs from CXR images, a Residual U-Net DL model was employed [21, 22]. This architecture was augmented using a multiscale image input pyramid for better intermediate feature representations with deep supervision (Supplementary Figure S1) [23]. To train the network, lung fields were first manually segmented for a dataset of 100 CXRs, excluding heart shadows. Additionally, artifacts such as EKG leads, pacemakers, and other non-anatomical objects were manually segmented in this training set. These segmentations were used to train a second multiscale-input Residual U-Net model to generate artifact masks. A focal Tversky loss function was employed ($\alpha=0.3$, $\gamma=1.0$) to ensure a higher penalty to false positive results [24]. This was to avoid misidentification of high-intensity objects as lungs and to mitigate misclassification of lungs as unwanted artifacts. These models were then used to generate lung and artifact masks for the remaining 434 CXRs. Each of these masks was manually reviewed and errors in segmentation, if any, were corrected.

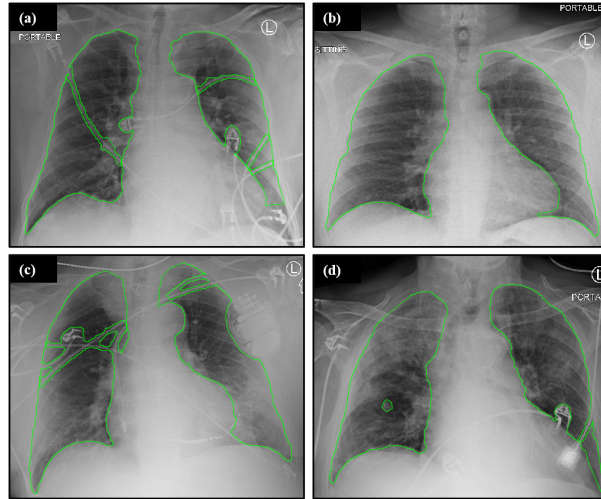


Figure 3. Representative CXRs studied. Displayed here are baseline CXRs taken from patients that later (a) required mechanical ventilation, (b) did not require ventilation, (c) survived the disease, and (d) did not survive. Green contours represent computationally-generated lung segmentations excluding non-anatomic artifacts such as wires.

Table 2. COVID-19 positive patient outcome table

Age		Number of COVID-19 positive patients	Number requiring mechanical ventilation	Number deceased
10-19 (N=1)	Male	1	0	0
	Female	0	0	0
20-29 (N=16)	Male	8	0	0
	Female	8	1	1
30-39 (N=37)	Male	23	6	2
	Female	14	2	2
40-49 (N=54)	Male	34	8	4
	Female	20	3	2
50-59 (N=84)	Male	45	15	11
	Female	39	10	5
60-69 (N=74)	Male	43	22	17
	Female	31	16	10
70-79 (N=41)	Male	24	13	12
	Female	17	9	7
80+ (N=31)	Male	18	4	8
	Female	13	0	3
Total (N=338)	Male	196	68	54
	Female	142	41	30

Experiment 1: Outcome classification using convolutional neural networks

Convolutional neural networks (CNNs) were employed to predict future mechanical ventilation requirement and patient mortality from the baseline CXRs. Utilizing the earlier-described image processing pipelines, lung and artifact segmentation was performed. Additional preprocessing steps included cropping of the full CXR to a tight boundary around the lungs, resizing of input images to 224 by 224 pixels, and the application of min-max normalization to rescale image intensity values between 0 and 1.

For each classification experiment, ResNet-18, ResNet-34, and ResNet-50 architectures were trialed [25]. Pre-trained weights were utilized in model training, and data augmentation techniques such as flipping, rotation, and translation were used to reduce the potential for overfitting. The fully-connected (FC) layer of each architecture was replaced by a custom layer with an input size of 512 by 1 (no clinical variables included) or 514 by 1 (patient age and sex included) and an output size of 2 by 1 to match our desired binary classification scheme. The FC layer was trained without the use of pre-trained weights. Dropout layers with a probability of 0.1 were included after FC layers to improve generalizability of classification. For each model, a binary cross-entropy loss function and an Adam optimizer with a learning rate of 0.00001 were used for network training [26]. The learning rate was decreased by a factor of 0.01 after each 10th epoch. The specific ResNet architecture chosen for each classification problem was determined based upon validation scoring for each tested architecture.

To classify ventilation requirement, training was performed on a set of 41 CXRs from patients who eventually required mechanical ventilation (*Group V*) and 41 CXRs from COVID-19 positive patients who did not (*Group NV*). Validation was performed on 10 CXRs from *Group V* and 86 CXRs from *Group NV*. Based on the validation results, a ResNet-34 architecture was chosen as the best performing network. Testing was performed on 62 CXRs from *Group V* and 92 CXRs from *Group NV*.

For mortality classification, training was performed on 27 CXRs from COVID-19 patients who did not survive (*Group NR*) and 27 CXRs from patients who recovered (*Group R*). Validation was performed on 10 CXRs from (*Group NR*) and 86 CXRs from (*Group R*). A ResNet-18 architecture was determined to produce the best results on validation. Testing was performed on 52 CXRs from (*Group NR*) and 138 CXRs from (*Group R*).

Experiment 2: Outcome classification using radiomic features

143 radiomic features from the Haralick, Gabor, Laws energy, histogram of gradients, and grey intensity feature families were computed for each baseline CXR [27–30]. Features were extracted solely from segmented lung fields, excluding any artifacts. For each radiomic feature, various statistics were calculated including measures of median, skewness, standard deviation, and kurtosis. The obtained statistics and clinical factors including patient age and sex were used for classifier construction.

To develop machine learning classifiers to predict future mechanical ventilation requirement and mortality, baseline CXRs were divided into the same training, validation, and testing sets used in

Experiment 1. First, the training set was used to train Random Forest (RF), Linear Discriminant Analysis, and Quadratic Discriminant Analysis classifiers [31, 32]. For each of 100 iterations in a 3-fold cross validation setting, feature reduction among radiomic and clinical features was performed on the training set using a Wilcoxon rank sum test, student's t-test, or a maximum relevance minimum redundancy approach [33]. Highly correlated features (identified using a correlation threshold of 0.9) were removed to reduce redundancy. Validation experiments were then performed to identify the best classifier. Finally, the chosen classifiers, trained on the training set were evaluated on the distinct testing set of CXRs.

Based upon the results of validation experiments, RF classifiers were used for both COVID-19 mechanical ventilation requirement and mortality prediction. For ventilation classification, eight radiomic features were used while six were selected for mortality classification (Table S1).

Experiment 3: Outcome classification using convolutional neural networks and radiomic-map embedding

The radiomic feature statistics from Experiment 2 were used to create radiomic-embedded feature maps for each CXR. t-Distributed Stochastic Neighbor Embedding (random state=1) was employed to perform feature reduction and to convert radiomic data to a 2D representation [34]. The normalization procedure is detailed in Supplementary Section I.

To assess the predictive capability of a model trained using both these radiomic-embedded feature maps and CXR images as inputs, the same general procedure employed in Experiment 1 was used. A key difference was a change in the first input convolution filter of each ResNet architecture to receive a 2-channel rather than a 3-channel input. Here our first channel was the CXR and the second was the corresponding radiomic-embedded feature map. This new input layer did not use pre-trained weights. All other network configurations are identical to those described in Experiment 1. A ResNet-50 architecture and ResNet-34 architecture were determined by validation to perform best for mechanical ventilation requirement and mortality prediction, respectively. Dataset splits of each of these classifiers were identical to those detailed in Experiment 1.

Evaluation of all classifiers in Experiments 1 through 3 was performed using a bootstrap resampling approach on the test set over 100 iterations.

Class Activation Mapping of DL Models

Class Activation Maps (CAMs) were also generated for Experiment 1 using network outputs prior to the global average pooling layer in each ResNet architecture. These CAMs enable a degree of visualization of the areas in an image that the model used to make predictions.

Results

Results and 95% confidence intervals for Experiments 1, 2, and 3 are summarized in Table 3 and Table 4.

In Experiment 1, a ResNet-34 model trained to predict future mechanical ventilation requirement had an AUC of 0.842, a specificity of 73%, and a sensitivity of 83% on the testing dataset. A ResNet-18 model trained to predict mortality yielded an AUC of 0.639, a specificity of 66%, and a sensitivity of 50% on the testing dataset. Representative CAMs are shown in Figure 4. An expert reader (J.G, 15 years of experience) noted diffuse, bilateral patchy infiltrates most notable in the middle and lower lung zones on both CXR images. These findings align with our CAM findings of high network activations within lung fields, predominantly in the middle and lower lung zones.

Table 3. Mechanical ventilation requirement classifier results

Classification Type	Clinical Features	Sensitivity	Specificity	AUC
ResNet-34 – CXR	None	0.828±0.008	0.725±0.007	0.842±0.041
	Age and Sex	0.691±0.009	0.648±0.007	0.755±0.005
Random Forest – Radiomic Features	None	0.964±0.006	0.615±0.013	0.867±0.008
	Age and Sex	0.972±0.006	0.632±0.014	0.905±0.005
ResNet-50 – CXR + Radiomic Embedding Map	None	0.907±0.005	0.705±0.006	0.897±0.004
	Age and Sex	0.907±0.005	0.706±0.006	0.903±0.004

For Experiment 2, an RF classifier, trained to predict need for mechanical ventilation, yielded an AUC of 0.905, a specificity of 63%, and a sensitivity of 97% on the testing dataset. An RF classifier was also used to predict mortality in COVID-19 positive patients and had an AUC of 0.926, a specificity of 69% and a sensitivity of 100% on the testing dataset. The top radiomic features used for predicting mechanical ventilation requirement and mortality were the Laws S5L5 filter responses and Haralick correlation, respectively (Figure 5).

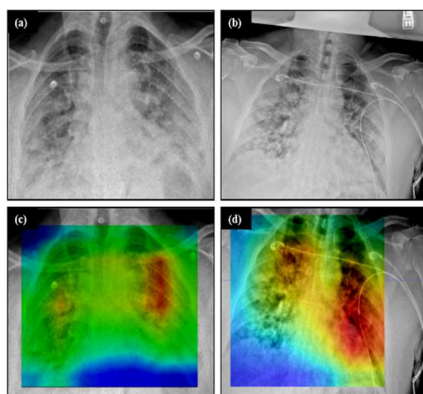


Figure 4. Representative class activation maps for deep learning models. The baseline CXRs depicted in (a) and (b) along with their respective CAMs in (c) and (d) are from two patients that later required mechanical ventilation. CAMs in (c) and (d) depict high levels of activation in the left middle and lower lung zones, in concordance with an expert reader’s interpretation of the respective CXRs shown in (a) and (b). Also note that activations are primarily within lung fields and exclude other areas of the images.

Table 4. Mortality prediction classifier results

Classification Type	Clinical Features	Sensitivity	Specificity	AUC
ResNet-18 – CXR	None	0.503±0.014	0.663±0.007	0.639±0.008
	Age and Sex	0.444±0.014	0.548±0.008	0.506±0.010
Random Forest – Radiomic Features	None	1.000±0.000	0.691±0.010	0.926±0.005
	Age and Sex	0.889±0.032	0.804±0.017	0.925±0.007
ResNet-34 – CXR + Radiomic Embedding Map	None	0.916±0.007	0.435±0.007	0.732±0.007
	Age and Sex	0.700±0.011	0.615±0.007	0.756±0.007

For Experiment 3, a ResNet-50 model trained to predict future mechanical ventilation requirement had AUC of 0.903, a specificity of 71%, and a sensitivity of 91% on the testing dataset. A ResNet-34 model trained to predict mortality yielded an AUC of 0.756, a specificity of 62%, and a sensitivity of 70% on the testing dataset. For both predictions, these models had higher prediction confidence than those reported for Experiment 1 (Figure 6).

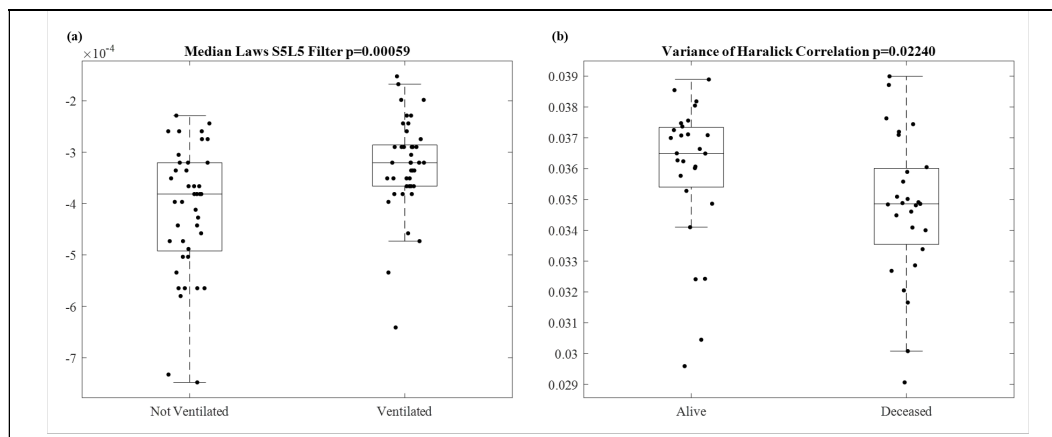


Figure 5. Radiomic classification features. (a) visualizes the median of the Laws S5L5 filter response for the ventilation requirement prediction dataset. (b) displays the variance of the Haralick correlation feature for the mortality prediction dataset. *p*-values are calculated using a Wilcoxon rank-sum test

Discussion

As the COVID-19 pandemic continues to unfold, there will be a growing need for useful interpretations of CXRs. In this work we have presented models for baseline CXRs that demonstrate high sensitivities in predicting future mechanical ventilation requirement ($\leq 97\%$) and mortality ($\leq 100\%$). For these predictions of disease outcomes, radiomic classifiers had higher

sensitivities than those yielded by DL. However, we did report higher specificities for prediction of mechanical ventilation requirement using DL classifiers with radiomic embedding (Table S2). Several non-imaging models have been proposed with high sensitivities for various clinical outcomes using biomarkers such as serum lactate dehydrogenase, C-reactive protein, lymphocyte counts, and coagulation factors [13–17]. These models might be complemented by novel imaging-based approaches. The quantitative modeling of baseline CXRs is relatively unexplored and will be of particular importance for resource allocation if projected scarcity of ventilators and other supplies occurs [10].

Previous studies have applied DL to the analysis of COVID-19 CXRs [12, 19, 20, 35]. However, at least one study has reported potential deficiencies in these approaches, including insufficiencies in a commonly used public dataset, a neglect to segment lung fields, and a failure to account for large differences between disparate public datasets [35]. Previous studies have also not explicitly accounted for foreign objects in the lung fields such as buttons, clips, wires, etc., which can obscure pathological findings. Here, we have developed a unique pre-processing pipeline to segment lung fields from CXRs. We have further shown that our classifiers are effective in predicting COVID-19 outcomes in patients treated at multiple institutions, reflecting a degree of robustness in their predictive value.

The high middle and lower lung activations observed in network CAMs are consistent with studies reporting lower lobe lung findings on both CT and CXR (Figure 4) [4–6]. In the CAMs presented in Figure 4, high network activations are visualized in areas where a radiologist had independently identified lung opacities, providing evidence that our DL models are using pathology-relevant features to predict patient outcomes.

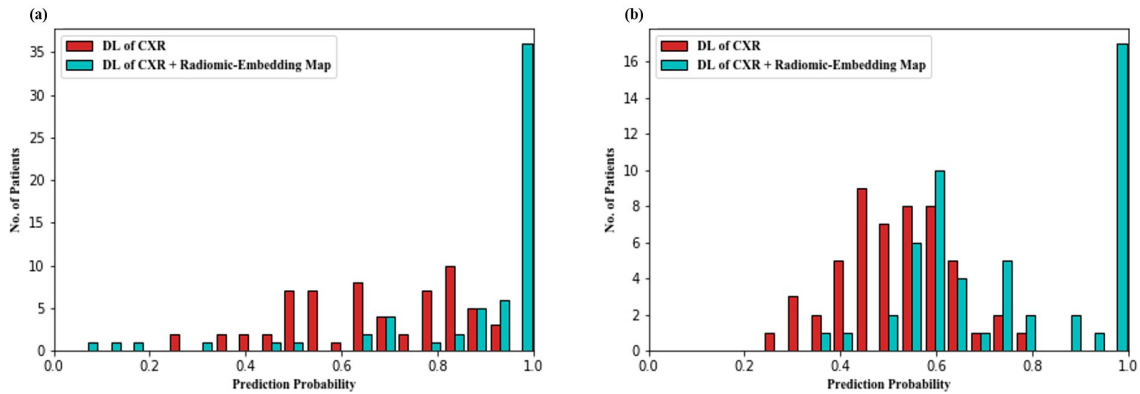


Figure 6. Prediction probabilities for deep learning models. (a) visualizes prediction probabilities generated for CXRs from patients that later required mechanical ventilation. (b) visualizes prediction probabilities for CXRs from patients that died.

Using an integrated model that incorporates both baseline imaging and the associated radiomic-embedded feature maps, we demonstrated an improvement in outcome prediction results over use of baseline image-based DL models alone (Figure 6). The generation of a radiomic-embedded feature map for DL classification is a novel approach in CXR analysis and may be used in future studies to augment DL approaches. While most learning approaches assume independence between prediction variables, DL considers the ‘relative arrangement’ of primitives such as that of image pixels. To increase the versatility of CNNs, we first embedded radiomic statistics in a

reduced dimensional space, clustered similar features together, and then used the embedding to obtain a pseudo image. This pseudo image was inputted into our classifiers in addition to the original CXR scan. This fusion framework can help assess feature importance and may also be extended to other clinical parameters. Both radiomic and radiomic embedding approaches can give insight into what features of a patient’s CXR are significant in making predictions, and the use of either can be more informative to a physician than exclusively DL approaches.

There are certain limitations in our work. First, we used baseline CXRs that are likely to be nonuniform in the interval between COVID-19 infection and image acquisition. While our data is representative of the clinical reality of patients receiving baseline CXRs at varying timepoints in the course of their disease, future studies might build improved time-to-event prediction models using data with a more uniform temporal distribution. Furthermore, we are limited in the number of clinical features studied and our models might benefit from including co-morbidities such as a history of cancer, chronic obstructive pulmonary disease, hypertension, etc. The inclusion of co-morbidities and other laboratory variables might further improve our models [13–17]. Finally, future work will be helpful in demonstrating the robustness of these classification models in the broader context of COVID-19 treatment in other hospitals and locations.

Conclusion

In summary, we have presented a complete pipeline for computational evaluation of CXR in COVID-19 patients. Both radiomic and DL classification models enable us to predict mechanical ventilation requirement and mortality from baseline CXRs. Furthermore, we demonstrate the improvement that a novel radiomic embedding approach has on DL predictions of COVID-19 outcomes. We posit that the ability to make early predictions of disease outcomes may aid in triage, clinical decision-making, and efficient hospital resource allocation as the COVID-19 pandemic progresses.

List of Abbreviations

COVID-19: Coronavirus disease 2019
CXR: Chest radiograph (x-ray)
DL: Deep Learning
2D: 2-dimensional
SBUH: Stony Brook University Hospital
NBIMC: Newark Beth Israel Medical Center
RT-PCR: Reverse transcriptase polymerase chain reaction
CNN: Convolutional neural network
FC: Fully-connected
RF: Random forest
LDA: Linear discriminant analysis
QDA: Quadratic discriminant analysis
CAM: Class activation map
AUC: Area under the receiving operator characteristic curve

Acknowledgements

Research reported in this publication was supported by the Office of the Vice President for Research and Institute for Engineering-Driven Medicine Seed Grants, 2019 at Stony Brook University. JB supported by NIGMS T32GM008444.

Notes

The authors declare no conflicts of interest. The Institutional Review Board approved this study to be a non-human subjects research study. All data was de-identified prior to any analysis.

This article has been submitted to *European Radiology*.

References

1. Dong E, Du H, Gardner L (2020) An interactive web-based dashboard to track COVID-19 in real time. *Lancet Infect Dis* 20:533–534. [https://doi.org/10.1016/S1473-3099\(20\)30120-1](https://doi.org/10.1016/S1473-3099(20)30120-1)
2. Chaganti S, Balachandran A, Chabin G, et al (2020) Quantification of Tomographic Patterns Associated with COVID-19 from Chest CT. 24
3. Toussie D, Voutsinas N, Finkelstein M, et al (2020) Clinical and Chest Radiography Features Determine Patient Outcomes In Young and Middle Age Adults with COVID-19. *Radiology* 201754. <https://doi.org/10.1148/radiol.2020201754>
4. Wen Z, Chi Y, Zhang L, et al (2020) Coronavirus Disease 2019: Initial Detection on Chest CT in a Retrospective Multicenter Study of 103 Chinese Subjects. *Radiol Cardiothorac Imaging* 2:e200092. <https://doi.org/10.1148/ryct.2020200092>
5. Wong HYF, Lam HYS, Fong AH-T, et al (2020) Frequency and Distribution of Chest Radiographic Findings in COVID-19 Positive Patients. *Radiology* 201160. <https://doi.org/10.1148/radiol.2020201160>

6. Yang R, Li X, Liu H, et al (2020) Chest CT Severity Score: An Imaging Tool for Assessing Severe COVID-19. *Radiol Cardiothorac Imaging* 2:e200047. <https://doi.org/10.1148/ryct.2020200047>
7. Ai T, Yang Z, Hou H, et al (2020) Correlation of Chest CT and RT-PCR Testing in Coronavirus Disease 2019 (COVID-19) in China: A Report of 1014 Cases. *Radiology* 200642. <https://doi.org/10.1148/radiol.2020200642>
8. ACR Recommendations for the use of Chest Radiography and Computed Tomography (CT) for Suspected COVID-19 Infection. <https://www.acr.org/Advocacy-and-Economics/ACR-Position-Statements/Recommendations-for-Chest-Radiography-and-CT-for-Suspected-COVID19-Infection>. Accessed 15 Jun 2020
9. Alhazzani W, Möller MH, Arabi YM, et al (2020) Surviving Sepsis Campaign: guidelines on the management of critically ill adults with Coronavirus Disease 2019 (COVID-19). *Intensive Care Med* 1–34. <https://doi.org/10.1007/s00134-020-06022-5>
10. Ranney ML, Griffeth V, Jha AK (2020) Critical Supply Shortages — The Need for Ventilators and Personal Protective Equipment during the Covid-19 Pandemic. *N Engl J Med* 382:e41. <https://doi.org/10.1056/NEJMp2006141>
11. Vaid A, Somani S, Russak AJ, et al (2020) Machine Learning to Predict Mortality and Critical Events in COVID-19 Positive New York City Patients. *Health Informatics*
12. Shi F, Wang J, Shi J, et al (2020) Review of Artificial Intelligence Techniques in Imaging Data Acquisition, Segmentation and Diagnosis for COVID-19. *ArXiv200402731 Cs Eess Q-Bio*
13. Liang W, Liang H, Ou L, et al (2020) Development and Validation of a Clinical Risk Score to Predict the Occurrence of Critical Illness in Hospitalized Patients With COVID-19. *JAMA Intern Med*. <https://doi.org/10.1001/jamainternmed.2020.2033>
14. Yan L, Zhang H-T, Goncalves J, et al (2020) An interpretable mortality prediction model for COVID-19 patients. *Nat Mach Intell* 2:283–288. <https://doi.org/10.1038/s42256-020-0180-7>
15. Ji D, Zhang D, Chen Z, et al (2020) Clinical Characteristics Predicting Progression of COVID-19. *Social Science Research Network, Rochester, NY*
16. Zhou Y, He Y, Yang H, et al (2020) Development and validation a nomogram for predicting the risk of severe COVID-19: A multi-center study in Sichuan, China. *PLoS ONE* 15:. <https://doi.org/10.1371/journal.pone.0233328>
17. Shang W, Dong J, Ren Y, et al The value of clinical parameters in predicting the severity of COVID-19. *J Med Virol* n/a: <https://doi.org/10.1002/jmv.26031>
18. Parekh VS, Jacobs MA (2019) Deep learning and radiomics in precision medicine. *Expert Rev Precis Med Drug Dev* 4:59–72. <https://doi.org/10.1080/23808993.2019.1585805>
19. Cohen JP, Morrison P, Dao L (2020) COVID-19 Image Data Collection. *ArXiv200311597 Cs Eess Q-Bio*
20. Ozturk T, Talo M, Yildirim EA, et al (2020) Automated detection of COVID-19 cases using deep neural networks with X-ray images. *Comput Biol Med*. <https://doi.org/10.1016/j.combiomed.2020.103792>
21. Ronneberger O, Fischer P, Brox T (2015) U-Net: Convolutional Networks for Biomedical Image Segmentation. *ArXiv150504597 Cs*
22. Zhang Z, Liu Q, Wang Y (2018) Road Extraction by Deep Residual U-Net. *IEEE Geosci Remote Sens Lett* 15:749–753. <https://doi.org/10.1109/LGRS.2018.2802944>
23. Lee C-Y, Xie S, Gallagher P, et al (2014) Deeply-Supervised Nets. *ArXiv14095185 Cs Stat*

24. Abraham N, Khan NM (2018) A Novel Focal Tversky loss function with improved Attention U-Net for lesion segmentation. ArXiv181007842 Cs
25. He K, Zhang X, Ren S, Sun J (2015) Deep Residual Learning for Image Recognition. ArXiv151203385 Cs
26. Kingma DP, Ba J (2017) Adam: A Method for Stochastic Optimization. ArXiv14126980 Cs
27. Haralick RM, Shanmugam K, Dinstein I (1973) Textural Features for Image Classification. IEEE Trans Syst Man Cybern SMC-3:610–621. <https://doi.org/10.1109/TSMC.1973.4309314>
28. Jain AK, Farrokhnia F (1991) Unsupervised texture segmentation using Gabor filters. Pattern Recognit 24:1167–1186. [https://doi.org/10.1016/0031-3203\(91\)90143-S](https://doi.org/10.1016/0031-3203(91)90143-S)
29. Laws KI (1980) Textured Image Segmentation. University of Southern California
30. Dalal N, Triggs B (2005) Histograms of oriented gradients for human detection. In: 2005 IEEE Computer Society Conference on Computer Vision and Pattern Recognition (CVPR'05). pp 886–893 vol. 1
31. Tin Kam Ho (1998) The random subspace method for constructing decision forests. IEEE Trans Pattern Anal Mach Intell 20:832–844. <https://doi.org/10.1109/34.709601>
32. Hastie T, Tibshirani R, Friedman JH (2009) The Elements of Statistical Learning: Data mining, Inference, and Prediction, 2nd ed. New York: Springer
33. Peng H, Long F, Ding C (2005) Feature selection based on mutual information criteria of max-dependency, max-relevance, and min-redundancy. IEEE Trans Pattern Anal Mach Intell 27:1226–1238. <https://doi.org/10.1109/TPAMI.2005.159>
34. Sharma A, Vans E, Shigemizu D, et al (2019) DeepInsight: A methodology to transform a non-image data to an image for convolution neural network architecture. Sci Rep 9:1–7. <https://doi.org/10.1038/s41598-019-47765-6>
35. Maguolo G, Nanni L (2020) A Critic Evaluation of Methods for COVID-19 Automatic Detection from X-Ray Images. ArXiv200412823 Cs Eess
36. Alkhouli M, Nanjundappa A, Annie F, et al (2020) Sex Differences in COVID-19 Case Fatality Rate: Insights From a Multinational Registry. Mayo Clin Proc. <https://doi.org/10.1016/j.mayocp.2020.05.014>
37. Wei X, Xiao Y-T, Wang J, et al (2020) Sex Differences in Severity and Mortality Among Patients With COVID-19: Evidence from Pooled Literature Analysis and Insights from Integrated Bioinformatic Analysis

Supplementary Section

1. t-Distributed Stochastic Neighbor Embedding normalization

The chosen normalization procedure utilized the minimum value for each feature independently (Min_j), and the global maximum (Max) to rescale values logarithmically between 0 and 1. This is formulated as follows where X_{tr} is the training dataset and $(j,:)$ refers to all samples of the j^{th} radiomic feature:

$$\begin{aligned} Min_j &= \min X_{tr}(j,:) \\ X_{tr}(j,:) &\leftarrow \log(X_{tr}(j,:) + |Min_j| + 1) \\ Max &= \max(X_{tr}) \\ X_{tr}(j,:) &\leftarrow \frac{X_{tr}(j,:)}{Max} \end{aligned}$$

The validation and test sets were then adjusted using the extrema values from the training set for normalization. If, after adjusting by the minimum values, any element of the validation or test set was less than 0, it was clamped at 0. Similarly, if after normalizing by the global maximum value any feature from the validation and test sets was above 1, it was clamped to 1.

2. False positive rates in mechanical ventilation predictions

In Table S2 we visualize the false positive rates for ventilation requirement prediction in Experiments 1 and 3. We see that false positive rates in mechanical ventilation requirement prediction are much higher in males than in females using radiomic-based RF classifiers. This might reflect the sex-based disparities in disease progression that have been reported in other studies for COVID-19 [36, 37]. Future studies might further investigate any differences in disease outcome prediction capabilities for male and female patients.

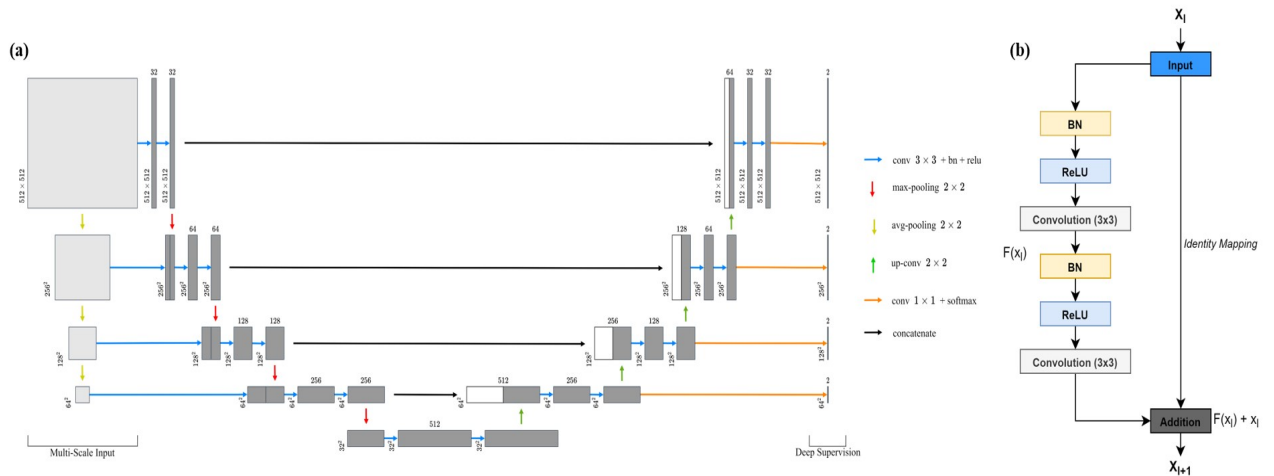


Figure S1. Network architecture for lung and image artifact segmentation. (a) visualizes our multiscale input Residual U-Net architecture. (b) displays an example residual block.

Table S1. Features used in radiomic classifiers

Classification Type	Clinical Features	Features Used in Classification	
Mechanical Ventilation Requirement	None	1. Laws L5E5	5. Gabor XY $\theta=0.785$ $\lambda=1.276$
		2. Gradient X	6. LawsS5W5
		3. Laws S5L5	7. Gradient Sobel yx
		4. Gradient Sobel xy	8. Gabor XY $\theta=1.571$ $\lambda=1.786$
	Age and Sex	1. LawsS5L5	5. Age
		2. Gabor XY $\theta=0.785$ $\lambda=1.276$	6. Laws S5W5
		3. Gradient Sobel xy	7. Gradient Diagonal
		4. LawsE5E5	8. Gradient X
Mortality	None	1. Haralick Correlation $W_s=5^*$	4. Gabor XY $\theta=0.785$ $\lambda=1.276$
		2. Laws E3E3	5. Haralick Energy $W_s=7^*$
		3. Gradient X	6. Raw Intensity
	Age and Sex	1. Haralick Correlation $W_s=5^*$	4. Laws E3E3
		2. Age	5. Gabor XY $\theta=0.785$ $\lambda=1.276$
		3. Sex	6. Gradient X

*Ws: Window size

Table S2. Mechanical ventilation requirement classifier false positive rates

Classifier Type	Sex	False Positive Rate	
		With Clinical Features	Without Clinical Features
Random Forest – Radiomic Features	Male	50%	50%
	Female	28%	34%
ResNet-50 – CXR + Radiomic Embedding Map	Male	31%	33%
	Female	28%	26%